




Article

# CuO-Ga<sub>2</sub>O<sub>3</sub> Thin Films as a Gas-Sensitive Material for Acetone Detection

Katarzyna Dyndał<sup>1</sup>, Arkadiusz Zarzycki<sup>2</sup> , Wojciech Andrysiewicz<sup>3</sup>, Dominik Grochala<sup>4</sup>,  
Konstanty Marszalek<sup>1</sup>  and Artur Rydosz<sup>1,\*</sup> 

<sup>1</sup> Department of Electronics, AGH University of Science and Technology, Al. Mickiewicza 30, 30-054 Kraków, Poland; kkoper@agh.edu.pl (K.D.); marszalek@agh.edu.pl (K.M.)

<sup>2</sup> Institute of Nuclear Physics Polish Academy of Sciences, PL-31342 Kraków, Poland; arkadiusz.zarzycki@ifj.edu.pl

<sup>3</sup> CB RTP SA, Waryńskiego 3A, 00-645 Warszawa, Poland; andrysiewicz@agh.edu.pl

<sup>4</sup> Department of Biocybernetics and Biomedical Engineering, AGH University of Science and Technology, Al. Mickiewicza 30, 30-054 Kraków, Poland; grochala@agh.edu.pl

\* Correspondence: rydosz@agh.edu.pl; Tel.: +48-126-172-594

Received: 11 May 2020; Accepted: 1 June 2020; Published: 2 June 2020



**Abstract:** The p-n heterostructures of CuO-Ga<sub>2</sub>O<sub>3</sub> obtained by magnetron sputtering technology in a fully reactive mode (deposition in pure oxygen) were tested under exposure to low acetone concentrations. After deposition, the films were annealed at previously confirmed conditions (400 °C/4 h/synthetic air) and further investigated by utilization of X-ray diffraction (XRD), X-ray reflectivity (XRR), energy-dispersive X-ray spectroscopy (EDS). The gas-sensing behavior was tested in the air/acetone atmosphere in the range of 0.1–1.25 ppm, as well as at various relative humidity (RH) levels (10–85%). The highest responses were obtained for samples based on the CuO-Ga<sub>2</sub>O<sub>3</sub> (4% at. Ga).

**Keywords:** gas sensors; acetone detector; thin-films; copper oxides; gallium oxides

## 1. Introduction

Gas detectors have constantly been developed over the last few decades, and the number of applications is still growing, from industrial to everyday life applications [1–6]. Generally, the gas sensors consist of few elements, such as active material, referred to as the gas-sensitive layer, and transducers, including electrodes, package, and front-end electronics. The gas-sensitive layers are based on different materials, and metal oxides are one of the most commonly used. Among them, copper oxide has become increasingly attractive. The copper oxide is a typical p-type semiconductor, it has been used as a base material for several applications, including solar energy cells [7], optoelectronics [8], catalysis [9,10], biosensors [11], supercapacitors [12], lithium ion batteries [13], electrochemical sensors [14], and gas sensors [15]. An actual review of CuO-based gas sensors was presented by the authors of [16], where various different deposition methods, target gases, and operating conditions were discussed. The CuO-based gas-sensing materials utilize a pure copper oxide, as well as copper oxide doped with various metals, e.g., Ag, Au, Cr, Pt, Sb, Si [17], Al [18], Fe, Li [19,20], Na [20], grapheme [21], Pd [22], Zn [23], and other oxides. Recently, the following compositions of copper oxide and other metal oxides (MOX) were reported, such as CuO/TiO<sub>2</sub> [24], CuO/CuS [25], ZnO/CuO [26–28], CuO/In<sub>2</sub>O<sub>3</sub> [29], CuO/NiO [30,31], WO<sub>3</sub>/CuO [32], rGO/CuO [33,34], PtO<sub>2</sub>/CuO [35], Fe<sub>2</sub>O<sub>3</sub>/CuO [36], CuO/SnO<sub>2</sub> [37–39], and CuO/CeO<sub>2</sub> [9,40].

The CuO-based gas sensors are used for detection of reducing gases and oxidizing gases, such as CO [41–45], H<sub>2</sub> [23,45–47], NH<sub>3</sub> [33,43], C<sub>6</sub>H<sub>6</sub> and C<sub>7</sub>H<sub>8</sub> [45,48], H<sub>2</sub>S [26,37,38,43], CH<sub>3</sub>OH and

$C_3H_6O$  [40],  $C_2H_5OH$  [43,49], and  $NO_2$  [41,43,45,50–52],  $SO_2$  [43,45],  $O_2$  [45], and  $CO_2$  [43], respectively. The responses are usually defined as the resistance ratio  $R_a/R_g$  or  $R_g/R_a$ , where  $R_a$  and  $R_g$  are electrical resistances in air and target gas, respectively. Apart from the common compositions mentioned above, a  $CuO-Ga_2O_3$  has not been reported to date. Therefore, in this paper, a  $CuO-Ga_2O_3$ -based gas sensor for enhanced acetone detection was presented.

$Ga_2O_3$ -based gas sensors have been reported since 1991 [53], and since then, gallium oxides have been studied as potential films in gas-sensing applications. There are several polymorphs of  $Ga_2O_3$  [54], such as the rhombohedral ( $\alpha-Ga_2O_3$ ), monoclinic ( $\beta-Ga_2O_3$ ), defective spinel ( $\gamma-Ga_2O_3$ ), cubic ( $\delta-Ga_2O_3$ ), and orthorhombic ( $\epsilon-Ga_2O_3$ ) structure, among which the most chemical and thermal stable under ambient conditions is  $\beta$ -polymorph [55]. Moreover, the various forms of low-dimensional crystalline  $Ga_2O_3$ , including nanowires (NWs) [56,57], nanobelts (NBs) [58], and nanosheets (NSHs) [59], are the subject of research.  $Ga_2O_3$  is an n-type semiconductor with an ultrawide-bandgap in the range of 4.2–5.3 eV [54,60,61].  $Ga_2O_3$  is an interesting material due to its high conductivity [62–64], optical transparency in ultraviolet and visible regions [65], and excellent photoluminescence property, which is a result of its defect-rich structure [66].  $Ga_2O_3$  sensors show fast response and recovery times, good reproducibility, low cross sensitivity to humidity, and short pre-ageing times [67]. Moreover, the  $Ga_2O_3$  has found a wide range of applications in various disciplines. Thin layers of gallium oxides have been used in solar cells as an ultrathin tunneling layer in the dye-sensitized solar cell, as well as in passivation layers on silicon solar cells, photodetectors [68,69], and electronic devices [70]. Also, a lot of reported works have focused on gas-sensing behaviors based on this metal oxide, as well as its doped- $Ga_2O_3$  composite (i.e., Sn [71], Ce, Sb, W, Zn [72,73], Sn, Cu, N [74], Au [75]) and metal oxide/ $Ga_2O_3$  composite (i.e.,  $TiO_2$  [76],  $SiO_2$  [77],  $SnO_2$  [78],  $I_2O_3$ ,  $WO_3$  [79,80],  $ZnO$  [81],  $MgO$  [82]). Gas sensors based on  $Ga_2O_3$  are used for gas detection, e.g.,  $C_2H_5OH$  and  $C_3H_5OH$  [79,83],  $C_2H_4$  [72],  $H_2$  [61,63,79],  $O_2$  [72,84],  $NO_2$  [76],  $CO$  [76,79,85], and  $NH_3$  [79,86,87].

Several techniques were used to deposit or grow  $Ga_2O_3$  thin films, e.g., vapor-vapor-liquid-solid [62], chemical vapour deposition [88], spray pyrolysis [89], molecular beam epitaxy [90], electronic beam evaporation [91], pulsed laser deposition [92], magnetron sputtering [68], sol-gel [93] and vacuum thermal evaporation [66], plasma-enhanced atomic layer deposition [65], and atomic layer [94].

As previously mentioned,  $CuO-Ga_2O_3$  is a p-type/n-type heterostructure, where the base material ( $CuO$ ) has bandgap in the range 1.2–1.9 eV depending on the crystalline phase and stoichiometry [95,96], and the upper layer ( $Ga_2O_3$ ) has been reported in the range 4.2–5.3 eV of the bandgap. The application of p-type  $CuO$  and n-type  $ZnO$  heterostructure is well known with all of the advantages in gas sensor technology. The system designed for this study looked very similar and had similar advantages and similar improvement in sensing performance, especially for higher  $Ga_2O_3$  content. Electronic effects, such as the charge carrier separation or increased interfacial potential barrier energy of such system, are affected by the electronic properties of the system, leading to better sensitivity of the sensor on the sub-ppm level.

The  $Ga_2O_3$ -based gas sensors are shown in Table 1. For example, the authors of [83] investigated the impact of air humidity on the detection of gases such as  $H_2$ ,  $C_2H_4$ , and  $C_3H_5OH$ . The tests were carried out for 200 ppm and 500 ppm concentrations of  $H_2$ ,  $C_3H_5OH$ , and  $C_2H_4$ , respectively, in dry and wet air (15% RH) at temperatures in the range from 480 °C to 640 °C.  $C_3H_5OH$  studies have indicated that the sensitivity is higher in dry air compared to wet air and decreases as the temperature increases. Similar behaviors were observed for  $C_2H_4$ . For acetone, the sensor response was 17 and 11 (resistance ratio) at 550 °C in dry and wet air, respectively. In contrast, for the same temperature, the sensor response to  $H_2$  was 24 and 15 for dry and wet air. The obtained results for the  $H_2$  indicate that the presence of moisture at temperatures below 600 °C inhibits the sensing reaction. In [79], Paul et al. presented a comparison of  $Ga_2O_3$ -core/ $WO_3$ -shell nanostructures sensor responses with  $Ga_2O_3$  to such gases as  $C_2H_5OH$ ,  $C_3H_5OH$ ,  $NH_3$ ,  $CO$ , and  $H_2$ . For each gas, the sensitivity of the sensor was higher for  $Ga_2O_3$ -core/ $WO_3$  compared to pure  $Ga_2O_3$ . The author described this effect as a combination of the potential barrier-controlled carrier transport mechanism and the surface-depletion mechanism.

**Table 1.** The summary of the recently presented research results on gas-sensing applications.

Gas-Sensing Layer Material	Deposition Method	Target Gas	Concentration (ppm)	Response	Operating Temp. (°C)	Ref.
Ga <sub>2</sub> O <sub>3</sub>	screenprinting	C <sub>3</sub> H <sub>6</sub> O	200	17 <sup>A</sup> /11 <sup>A</sup>	550	[83]
Ga <sub>2</sub> O <sub>3</sub> -core/WO <sub>3</sub>	thermal evaporation	C <sub>3</sub> H <sub>6</sub> O	200	210 <sup>B</sup>	200	[79]
Ga <sub>2</sub> O <sub>3</sub>	screenprinting	C <sub>2</sub> H <sub>4</sub>	500	15 <sup>A</sup>	550	[83]
Ga <sub>2</sub> O <sub>3</sub>	thermal evaporation	C <sub>2</sub> H <sub>5</sub> OH	200	210 <sup>B</sup>	200	[79]
Ga <sub>2</sub> O <sub>3</sub> -core/WO <sub>3</sub>	thermal evaporation	C <sub>2</sub> H <sub>5</sub> OH	200	510 <sup>B</sup>	200	[79]
Ga <sub>2</sub> O <sub>3</sub>	sputtering techniques	C <sub>2</sub> H <sub>5</sub> OH	37	175 <sup>A</sup>	800	[67]
Ga <sub>2</sub> O <sub>3</sub>	screenprinting	H <sub>2</sub>	500	24/15 <sup>A</sup>	550	[83]
Ga <sub>2</sub> O <sub>3</sub>	vapor-liquid solid	H <sub>2</sub>	100	3.4 <sup>C</sup>	300	[63]
Ga <sub>2</sub> O <sub>3</sub>	sputtering techniques	CH <sub>4</sub>	5000	7 <sup>A</sup>	800	[97]
Ga <sub>2</sub> O <sub>3</sub> -core/WO <sub>3</sub>	thermal evaporation	H <sub>2</sub>	1000	310 <sup>B</sup>	200	[79]
Ga <sub>2</sub> O <sub>3</sub>	thermal evaporation	H <sub>2</sub>	1000	110 <sup>B</sup>	200	[79]
Ga <sub>2</sub> O <sub>3</sub>	thermal evaporation	NH <sub>3</sub>	100	160 <sup>B</sup>	200	[79]
Ga <sub>2</sub> O <sub>3</sub> -core/WO <sub>3</sub>	thermal evaporation	NH <sub>3</sub>	100	200 <sup>B</sup>	200	[79]
β-Ga <sub>2</sub> O <sub>3</sub>	drop casting method	NH <sub>3</sub>	100	50 <sup>D</sup>	RT	[86]
β-Ga <sub>2</sub> O <sub>3</sub>	spray pyrolysis	NH <sub>3</sub>	20	2500 <sup>F</sup>	30	[87]
Ga <sub>2</sub> O <sub>3</sub>	thermal evaporation	CO	100	120 <sup>B</sup>	200	[79]
Ga <sub>2</sub> O <sub>3</sub> -core/WO <sub>3</sub>	thermal evaporation	CO	100	210 <sup>B</sup>	200	[79]
Ga <sub>2</sub> O <sub>3</sub>	sputtering techniques	CO	5000	6 <sup>C</sup>	650	[85]
Ga <sub>2</sub> O <sub>3</sub> /Al <sub>2</sub> O <sub>3</sub>	two-step hydrothermal and calcining method	NO <sub>x</sub>	70	55 <sup>B</sup>	RT	[92]
Ga <sub>2</sub> O <sub>3</sub> /Al <sub>2</sub> O <sub>3</sub>	two-step hydrothermal and calcining method	NO <sub>x</sub>	70	7 <sup>B</sup>	RT	[98]
Ti-O <sub>2</sub> -Ga <sub>2</sub> O <sub>3</sub>	sol-gel method	NO <sub>2</sub>	10	3.5 <sup>E</sup>	200	[86]
Ga <sub>2</sub> O <sub>3</sub>	chemical thermal evaporation method	O <sub>2</sub>	5	10 <sup>G</sup>	300	[99]
Ga <sub>2</sub> O <sub>3</sub>	chemical thermal evaporation method	CO	500	5 <sup>G</sup>	100	[99]
TiO <sub>2</sub> -Ga <sub>2</sub> O <sub>3</sub>	sol-gel method	CO	400	7 <sup>E</sup>	200	[76]

<sup>A</sup>  $R_0/(R_0 + R_a)$ , <sup>B</sup>  $(R_0/R_a) \cdot 100\%$ , <sup>C</sup>  $R_a/R_0$ , <sup>D</sup>  $(R_a - R_0)/R_0 \cdot 100\%$ , <sup>E</sup>  $R_0/R_a$ , <sup>F</sup>  $(R_0 - R_a)/R_a \cdot 100\%$ , <sup>G</sup>  $(R_a - R_0)/R_0$ , where  $R_0$  and  $R_a$  are the resistance in carrier gas and  $R_a$  the resistance in the target gas, respectively.

## 2. Materials and Methods

### 2.1. Gas-Sensitive Layer Deposition

The gas-sensitive layers were based on copper oxide, which was previously confirmed as good gas-sensitive material [16,17,100], as well as on the copper oxide–gallium oxide composition with various Ga<sub>2</sub>O<sub>3</sub> contents. The films were deposited by the magnetron sputtering system with a glancing angle deposition technique and mosaic sputtering, where pure Ga (99.99999% purity) metal were placed on the pure Cu (99.9999%) magnetron target. The deposition conditions were previously fixed and are briefly presented in the Table 2.

**Table 2.** The summary of the deposition conditions.

Parameter	Value
Base pressure	$1 \times 10^{-6}$ mbar
Deposition pressure	$2 \times 10^{-2}$ mbar
Target to substrate distance	60 mm
Deposition temperature	100 °C
Deposition mode	fully reactive, deposition at pure oxygen
Presputtering time	10 min
Presputtering power	100 W
Sputtering time	20 min
Sputtering power	50 W
Oxygen flow	20 sccm

### 2.2. Gas-Sensing Measurements

The gas-sensing measurement system consisted of a few elements: The quartz-tube oven with an internal heater and temperature control unit, gas-dosing lines equipped with mass flow controllers 1179B (MKS Instruments, Andover, MA, USA), and the resistance measurement unit, which consisted of an electrometer (34401A HP, Keysight, MA, USA) and target gas canisters with 5 ppm of acetone (Air Products, Hershaw, UK). The gas-sensing measurement system was previously described in detail [101] The gas-sensing measurements were performed at various temperatures and 50% relative humidity (RH) level. Figure 1 shows the measurement system. The gas sensor response (S) was defined as the resistance ratio  $S = R_{\text{gas}}/R_{\text{air}}$ , where  $R_{\text{gas}}$  and  $R_{\text{air}}$  are electrical resistances in gas and air, respectively.

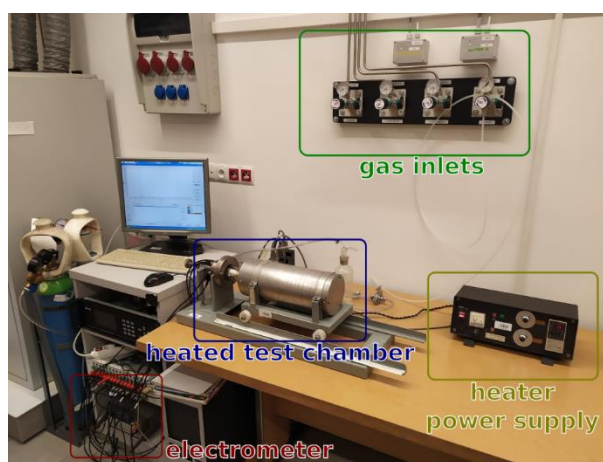


**Figure 1.** The measurement setup for gas-sensing characteristics. Reprinted from [101] CC BY 4.0.

### 2.3. EDS, XRD and XRR

The chemical composition of the samples was studied with scanning electron microscopy (Vega Tescan 3, Vienna, Austria) equipped with an X-ray spectroscopy (EDS) spectrometer (Bruker XFlash 610M, Vienna, Austria). For each sample, the EDS spectroscopy measurements were done for several arbitrary points, which were chosen on the surface of the sample. Additionally, maps with a scan size of around  $10 \times 10 \mu\text{m}$  were performed to study elements distribution. The acquisition time for single-point measurement and map were 5 min and 1 h, respectively.

The X-ray diffraction (XRD) and X-ray reflectivity (XRR) measurements were performed with an X'PertPro PANalytical diffractometer equipped with an X-ray source with a Cu anode operating at 40 kV and 30 mA. The XRR data were collected for the  $\omega$  angle between 0.2–2.0 degrees for 12 h for a sample to ensure sufficient statistics. The XRD  $\theta/2\theta$  patterns were gathered for a  $2\theta$  angle between 30 degrees and 90 degrees for 12 h for each sample. Additionally, in order to reduce signal from the Si wafer, a scattering vector was tilted by an angle of 3 degrees with respect to the diffraction plane. Details about measurement conditions have been described by the authors of [102,103]. The analysis of the obtained diffraction patterns was performed with FullProf software [104].

## 3. Results and Discussion

### 3.1. Characterization

#### 3.1.1. SEM

The EDS chemical composition analysis showed the presence of Si, O, Cu, and Ga elements in all samples, together with signals from C and N arising from sample contamination from the air. From the point of view of this study, the relative composition of copper and gallium was the most important factor. Hence, in this study, EDS analysis was restricted to those elements only. Table 3 shows the relative atomic compositions for Cu and Ga elements.

**Table 3.** Atomic concentration of copper and gallium from X-ray spectroscopy (EDS).

CuO-Ga <sub>2</sub> O <sub>3</sub>	Cu at.%	dCu at.%	Ga at.%	dGa at.%
S1	95.93	3.05	4.03	11.24
S2	92.42	3.08	7.58	7.60
S3	84.45	3.315	16.55	5.10

Figure 2a shows an exponential increase of gallium concentration between the samples, where the concentration changed between ~4 at.% and ~16 at.%. The Ga concentration in the sample was doubled as compared to the previous sample. A typical distribution of Cu and Ga elements is presented in Figure 2b based on the sample S3. In Figure 2b, blue indicates Cu, and magenta indicates Ga. The map confirms the homogeneous distribution of both elements and a higher concentration of copper as compared to gallium. Because there were no visible differences in elements distribution between samples containing different amount of gallium, only maps for the sample with the highest Ga concentration are presented in the paper, and all distributions are included in the Supplementary Materials Section.



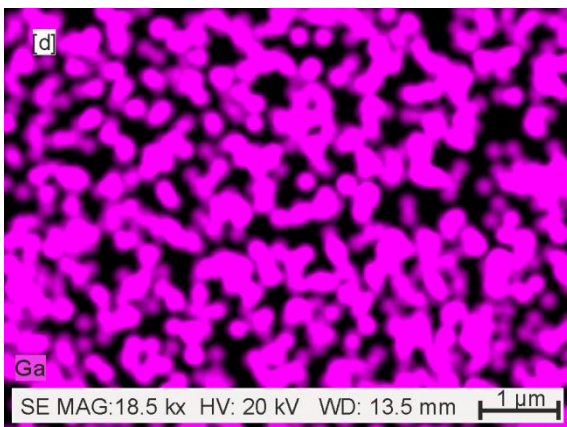
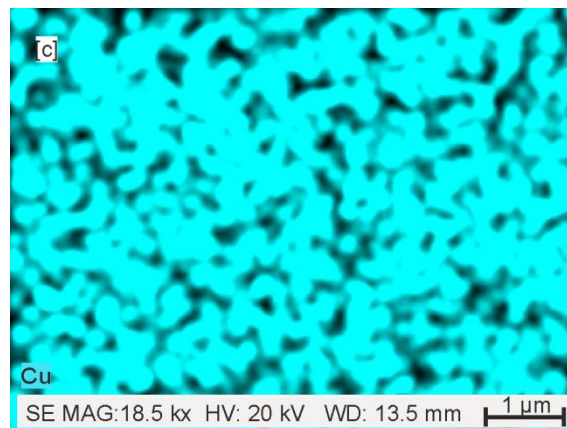
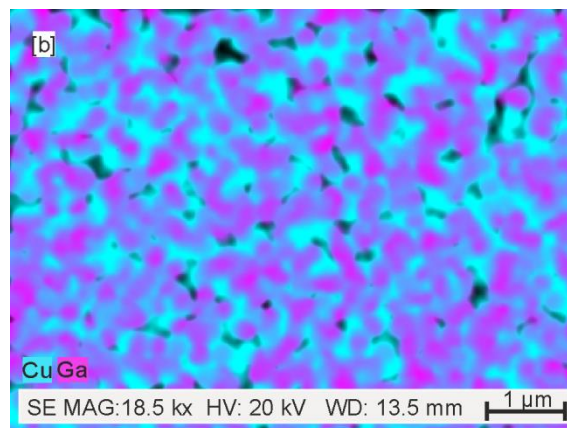
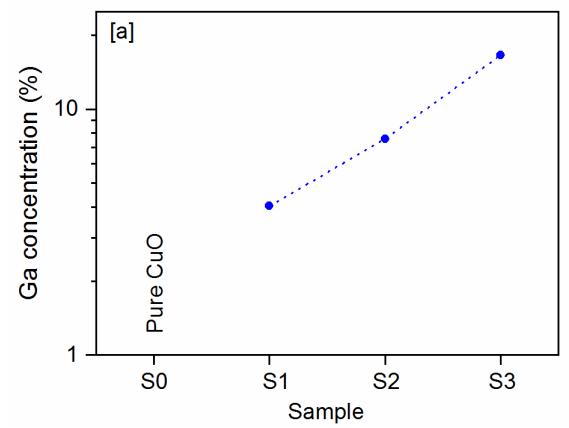


**Figure 2.** Gallium concentration (a), distribution map of sample S3 for Cu and Ga elements (b), and distribution maps of only Cu (c) and only Ga (d) elements for the same sample.

### 3.1.2. XRD/XRR

The X-ray reflectometry analysis showed that the samples had a thickness in the range of 60–70 nm, except the sample with the largest concentration of Ga, where the layer thickness was 40 nm. The various thicknesses were the consequence of the deposition time, which was kept constant (20 min) to keep the same deposition parameters for various gallium metal dopants placed on the copper magnetron target. The obtained results are presented in Figure 3 together with the spectra gathered for CuO:Ga<sub>2</sub>O<sub>3</sub> (sample S4, shown as an insert). The density in all studied cases was found to be around 5.6(1) g/cm<sup>3</sup> regardless of the gallium concentration. This value was significantly lower than that found for bulk copper(II) oxide, which was 6.31 g/cm<sup>3</sup>. Similarly, the lack of dependence of roughness with film composition was observed. The mean value was found to be relatively large, at around 3 nm.

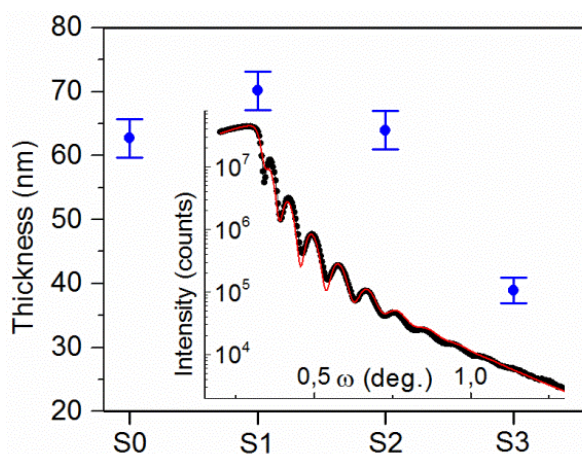


**Figure 3.** Films thicknesses for samples with different Ga concentration. In the insert, the XRR spectrum obtained for sample S4 with about 16 at.% of gallium is shown.

The diffraction patterns for all samples are presented in Figure 4. The continuous lines are the measurements results (thin irregular lines) together with fits (thicker and smooth lines). The longitudinal red and green lines indicate the position of Bragg maxima for the CuO and  $\beta$ -Ga<sub>2</sub>O<sub>3</sub> phases, while the back panel presents the powder X-ray diffraction patterns of those oxides. Both phases had a monoclinic crystal system with the C2/c and C2/m space group, respectively (ICSD card No. 00-045-0937 and ICSD card No. 00-041-1103). During the analysis, for the two samples with the smallest Ga amounts, only one phase of copper oxide was fitted, while for samples with about 8 at.% and 16 at.% of gallium, a small amount of  $\beta$ -Ga<sub>2</sub>O<sub>3</sub> was also found, meaning a sufficient signal from crystalline gallium(III) oxide was detected with XRD measurements. For those diffractograms, three fitting lines were included on the graph, indicating patterns for the CuO and  $\beta$ -Ga<sub>2</sub>O<sub>3</sub> phases and a total phase. Additionally, for samples doped with the largest amount of gallium, a shift in preferential grain orientation was clearly evident. The wide and intensive maxima observed for an angle around 35 deg., in case of sample S1 (CuO:Ga<sub>2</sub>O<sub>3</sub> with 4% at. Ga), became weak and small in samples strongly doped with gallium. Furthermore, a change in the pattern leading to a shift of the peak was found around 38 deg. due to the larger values and its separation from at least two individual Bragg maxima.

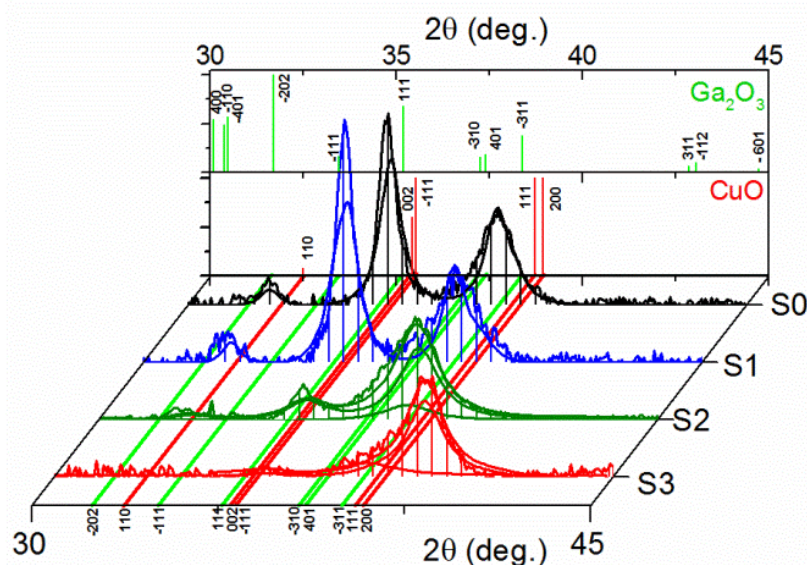


**Figure 4.** Diffraction patterns of CuO:Ga samples with fits and with marked positions of Bragg maxima for bulk CuO and  $\beta\text{-Ga}_2\text{O}_3$  phases (back panel).

Because of small amount of gallium oxide in the pattern, the crystallographic parameters used for this phase during the fitting procedure were from the crystallographic database and were kept constant during analysis. On the other hand, the parameters for copper oxide were varied and slow, and a systematic change with the increase of gallium concentration was observed. Figure 5 shows a change of cell volume with Ga concentration where a decrease from  $\sim 82 \text{ \AA}^3$  to  $\sim 80 \text{ \AA}^3$  is clearly seen. The insert of the graph shows dependence of cell parameters of  $a$ ,  $b$ ,  $c$  and  $\beta$  constants with gallium concentration. The dashed lines are values found in the database for the bulk sample. The most significant change was with the  $\beta$  angle, where a reduction of around  $1 \text{ deg.}$  was found for all studied samples, while the difference between the specific Ga concentration was uncertain. As mentioned previously, the reduction of cell volume is a consequence of the changes of the Ga concentration, which can be seen especially well for the sample S4 with the 16 at.% of Ga. Furthermore, with a shift of the  $a$  parameter, a strong (100) crystallographic texture was found in CuO:Ga $_2$ O $_3$  films with 8 at.% (sample S2) and 16 at.% Ga (sample S3). Also, for those samples, an increase of peaks widths was found.

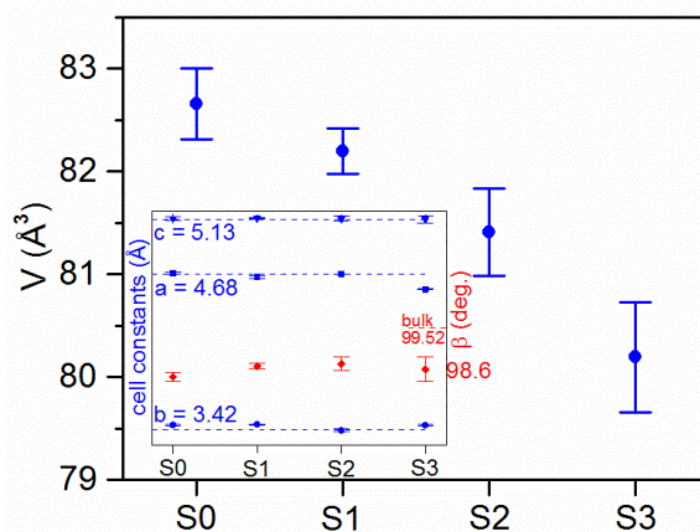


**Figure 5.** Changes in cell volume of CuO phase with an increase of gallium concentration. Insert presents the cell parameters of copper oxide.



An estimation of the size of crystallites was performed by applying a Scherrer formula. The Scherrer formula, linking coherence length ( $L_{\text{coh}}$ ) together with the width of Bragg's maxima ( $\omega$ ) found at  $2\theta$  angle for used wavelength  $\lambda$ , allowed us to estimate the size of crystallites:  $L_{\text{coh}} = k\lambda/\omega\cos\theta$ , where  $k$  is a Scherrer constant typically equal to 0.95 for thin films [102]. The samples S0 and S1 without and with small gallium concentration (i.e., pure CuO and CuO:Ga<sub>2</sub>O<sub>3</sub> with 4% at. Ga) had a mean grain size of 12–14 nm, while the S3 and S4 samples with 8 at.% and 16 at.%, respectively, showed a decrease of mean grain size to ~7 nm. Furthermore, the mean size of gallium(III) oxide crystallites for those two samples was found to be even lower, at around 5 nm. The XRD analysis allowed us to estimate the amount of crystalline  $\beta$ -Ga<sub>2</sub>O<sub>3</sub> phase in the spectra to be of several percents, i.e., 3(1)% and 5(1)% for S2 and S3 samples with Ga concentration of 8 at.% and 16 at.%, respectively.

### 3.1.3. Gas-Sensing Characteristics

The gas-sensing characteristics of the CuO-Ga<sub>2</sub>O<sub>3</sub>-based gas sensors under exposure to various acetone concentrations in time function, with gas-in/gas-out phases, are presented in Figure 6a–d. As can be observed, the p-n heterostructure made of p-type CuO and n-type Ga<sub>2</sub>O<sub>3</sub> reacted in increasing the resistance when acetone was introduced to the measurement cell and decreased the resistance in synthetic air. Therefore, the sensor response was defined as the resistance ratio  $R_{\text{gas}}/R_{\text{air}}$ , where  $R_{\text{gas}}$  and  $R_{\text{air}}$  are electrical resistance under exposure to acetone and synthetic air, respectively. The sensor response as a function of acetone concentration at 300 °C and 50% RH is presented in Figure 7. As can be noticed, the doping effect of Ga<sub>2</sub>O<sub>3</sub> to pure CuO slightly increased the sensor response in the 0.1–1.25 ppm of acetone. However, the highest responses were obtained for samples with lower gallium oxide content, i.e., around ~4% at. Therefore, further investigations will be focused on the experiments with 2–6% at. doping. Moreover, sample S1 exhibited 40% faster response time in comparison with pure CuO samples (Figure 8). All response/recovery times are shown in Table 4. The resistance changes measured at various relative humidity concentrations are presented in Figure 9. The fact that the gas-sensing performance of thin film-based sensors is correlated with humidity is widely known. However, as can be noticed, the fabricated sensors remained stable in the full range of various relative humidity due to the p-n structure. The relative resistance changes in the 10–90% relative humidity range were around ~30% for all samples. However, in the range, 50–90% of changes were below 5% which makes the developed sensors very attractive for utilization in the highly humidified samples, such as exhaled human breath analysis.

**Table 4.** Response and recovery times obtained for CuO and CuO:Ga films with different gallium concentrations at 1.25 ppm, 0.25 ppm, and 0.1 ppm acetone exposure.

Acetone → Concentration		1.25 ppm		0.25 ppm		0.1 ppm	
Samples ↓		$t_{\text{response}}$ [s]	$t_{\text{recovery}}$ [s]	$t_{\text{response}}$ [s]	$t_{\text{recovery}}$ [s]	$t_{\text{response}}$ [s]	$t_{\text{recovery}}$ [s]
S0	CuO	319	901	431	862	451	825
S1	CuO:Ga <sub>2</sub> O <sub>3</sub> (~4% at. Ga)	187	525	394	563	394	601
S2	CuO:Ga <sub>2</sub> O <sub>3</sub> (~8% at. Ga)	264	658	413	752	489	884
S3	CuO: Ga <sub>2</sub> O <sub>3</sub> (~16% at. Ga)	376	847	470	809	433	865

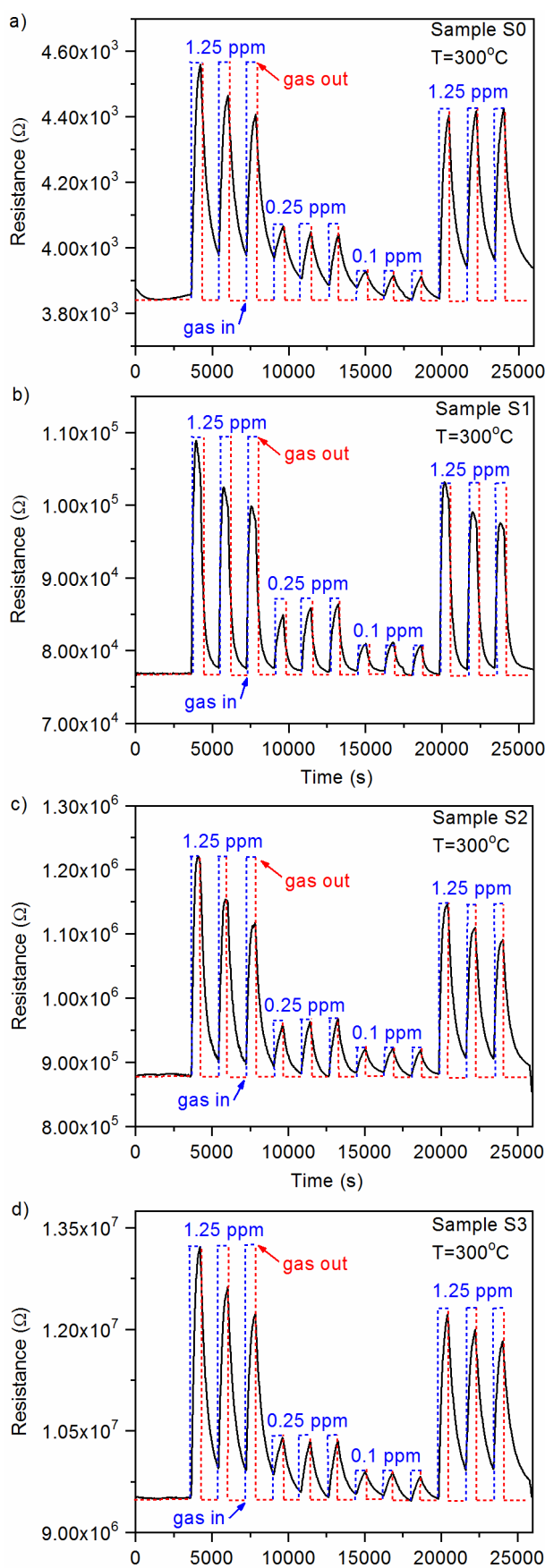


**Figure 6.** Sensor response as a function of acetone concentration at (a)  $300^{\circ}\text{C}$  and 50% RH for CuO (sample S0), (b) CuO:Ga films deposited with 4% at. (sample S1); (c) 8% at. (sample S2); (d) 16% at. (sample S3) of gallium concentration.

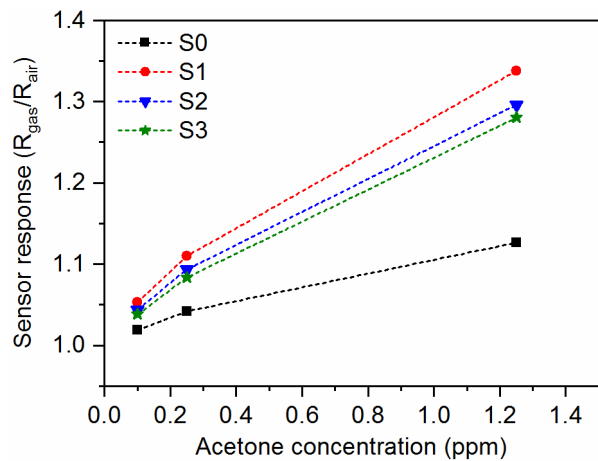


**Figure 7.** Sensor response as a function of acetone concentration at 300 °C and 50% RH for pure CuO (sample S0) and CuO:Ga films deposited with 4% at. (sample S1), 8% at. (sample S2), and 16% at. (sample S3) of gallium concentration.

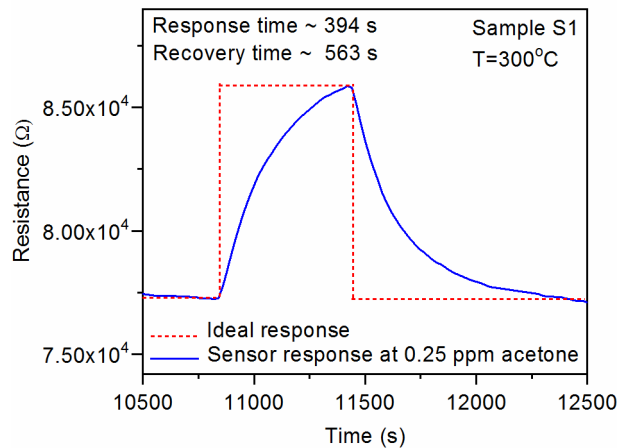


**Figure 8.** The response and recovery times at 300 °C for CuO:Ga<sub>2</sub>O<sub>3</sub> films (sample S1) with ~4% at. Ga at the exposition to 0.25 ppm acetone.

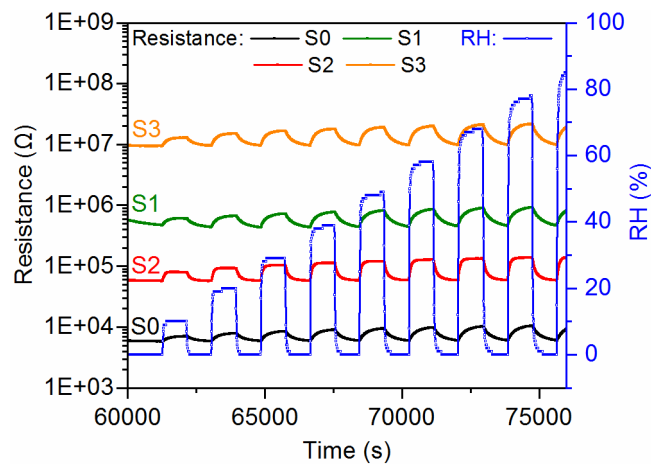


**Figure 9.** The resistance changes of the fabricated sensors S0–S4 measured at 300 °C at various relative humidity levels.

### 3.1.4. Response and Recovery Times

The response and recovery times are presented in the Table 4 as well as an example of the calculation is given in Figure 8. Briefly, in the gas-sensing applications, the response and recovery time (s) is defined as the time to reach a 90% variation of the sensor signal. In this study, resistance under exposure to target gas and air, respectively. It has to be underlined, that the obtained times are quite high and further works should be focused on the reduction of response and recovery time (s), for example by using noble metal dopings.

## 4. Conclusions

The GLAD magnetron sputtering was used for CuO-Ga<sub>2</sub>O<sub>3</sub> film deposition from the Cu:Ga mosaic target for gas sensor purposes. The sputtering conditions were presented for the thin CuO-Ga<sub>2</sub>O<sub>3</sub> deposition with an average deposition rate of about 2.5 nm/min. The sample structure was investigated by XRD, XRR, and EDS measurements. The content of gallium was determined to be 4 at.% to 16 at.%, and film density was found to be 5.6 g/cm<sup>3</sup> regardless of the gallium concentration. Diffraction patterns indicated Bragg peaks for the monoclinic phase of CuO for samples with a low Ga content, and CuO and β-Ga<sub>2</sub>O<sub>3</sub> monoclinic phases for samples with a higher Ga content. Also, the grain size changed from around 7 nm for a low content of gallium to 12–14 nm for samples with a higher content of gallium. For the measurements of the sensing properties of the CuO-Ga<sub>2</sub>O<sub>3</sub> system, all investigated samples were able to detect acetone on levels of 1.25 ppm, 0.25 ppm, and 0.1 ppm. The signal values are presented in Figure 8. The response and recovery times were high, however, it has to be underlined that the results were related to the measurement setup, in which a high volume quartz-glass tube was used. The advantage of this type of sensor is its low humidity influence on the signal level. In conclusion, according to the CuO-Ga<sub>2</sub>O<sub>3</sub> system review and our results, the design was properly designed to detect very low level acetone concentration sensors on ppm and even below ppm levels.

**Supplementary Materials:** The following are available online at <http://www.mdpi.com/1424-8220/20/11/3142/s1>, Figure S1: Gallium/copper concentrations: (a) distribution map of sample S1 for Cu and Ga elements, (b) distribution map of sample S2 for Cu and Ga elements, (c) distribution map of sample S3 for Cu and Ga elements.

**Author Contributions:** Conceptualization, A.R., K.D.; methodology, A.R., A.Z., W.A., K.M.; software, W.A., D.G.; validation, A.R., A.Z., K.D., W.A., K.M.; investigation, A.R., W.A., A.Z., K.D., K.M.; writing—original draft preparation, A.R., A.Z., K.D., K.M.; writing—review and editing, A.R., K.D., A.Z., K.M.; visualization, A.R., A.Z., K.D., supervision, A.R., K.M.; project administration, A.R. All authors have read and agreed to the published version of the manuscript.

**Funding:** This research was funded by the National Science Centre, Poland 2017/26/D/ST7/00355.

**Conflicts of Interest:** The authors declare no conflict of interest.

## References

1. Liu, X.; Cheng, S.; Liu, H.; Hu, S.; Zhang, D.; Ning, H. A Survey on Gas Sensing Technology. *Sensors* **2012**, *12*, 9635–9665. [CrossRef]
2. Moseley, P.T. Progress in the Development of Semiconducting Metal Oxide Gas Sensors: A Review. *Meas. Sci. Technol.* **2017**, *28*, 082001. [CrossRef]
3. Xu, K.; Fu, C.; Gao, Z.; Wei, F.; Ying, Y.; Xu, C.; Fu, G. Nanomaterial-Based Gas Sensors: A Review. *Instrum. Sci. Technol.* **2018**, *46*, 115–145. [CrossRef]
4. Nazemi, H.; Joseph, A.; Park, J.; Emadi, A. Advanced Micro-and Nano-Gas Sensor Technology: A Review. *Sensors* **2019**, *19*, 1285. [CrossRef]
5. Feng, S.; Farha, F.; Li, Q.; Wan, Y.; Xu, Y.; Zhang, T.; Ning, H. Review on Smart Gas Sensing Technology. *Sensors* **2019**, *19*, 3760. [CrossRef]
6. Guan, W.; Tang, N.; He, K.; Hu, X.; Li, M.; Li, K. Gas-Sensing Performances of Metal Oxide Nanostructures for Detecting Dissolved Gases: A Mini Review. *Front. Chem.* **2020**, *8*, 76. [CrossRef]
7. Iqbal, K.; Ikram, M.; Afzal, M.; Ali, S. Efficient, Low-Dimensional Nanocomposite Bilayer CuO/ZnO Solar Cell at Various Annealing Temperatures. *Mater. Renew. Sustain. Energy* **2018**, *7*, 4. [CrossRef]

8. Song, H.J.; Seo, M.H.; Choi, K.W.; Jo, M.S.; Yoo, J.Y.; Yoon, J.B. High-Performance Copper Oxide Visible-Light Photodetector via Grain-Structure Model. *Sci. Rep.* **2019**, *9*, 1–10. [[CrossRef](#)]
9. Di Benedetto, A.; Landi, G.; Lisi, L. Improved CO-PROX Performance of CuO/CeO<sub>2</sub> Catalysts by Using Nanometric Ceria as Support Almerinda. *Catal. Artic.* **2018**, *8*, 209.
10. Poreddy, R.; Engelbrekt, C.; Riisager, A. Copper Oxide as Efficient Catalyst for Oxidative Dehydrogenation of Alcohols with Air. *Catal. Sci. Technol.* **2015**, *5*, 2467–2477. [[CrossRef](#)]
11. Electrode, N.; Sridara, T.; Upan, J.; Saianand, G.; Tuantranont, A. Non-Enzymatic Amperometric Glucose Sensor Based on Carbon Nanodots and Copper Oxide. *Sensors* **2020**, *20*, 808.
12. Sayson, L.V.A.; Lopez, J.M.; Estacio, E.S.; Salvador, A.A.; Somintac, A.S. Nanostructured CuO Thin Film Deposited on Stainless Steel Using Spray Pyrolysis as Supercapacitor Electrode Nanostructured CuO Thin Film Deposited on Stainless Steel Using Spray Pyrolysis as Supercapacitor Electrode. *Mater. Res. Express* **2019**, *6*, 125551. [[CrossRef](#)]
13. Deng, Z.; Ma, Z.; Li, Y.; Li, Y.; Chen, L.; Yang, X.; Wang, H. Boosting Lithium-Ion Storage Capability in CuO Nanosheets via Synergistic Engineering of Defects and Pores. *Front. Chem.* **2018**, *6*, 428. [[CrossRef](#)]
14. Sundar, S.; Venkatachalam, G. Biosynthesis of Copper Oxide (CuO) Nanowires and Their Use for the Electrochemical Sensing of Dopamine. *Nanomaterials* **2018**, *8*, 823. [[CrossRef](#)] [[PubMed](#)]
15. Rydosz, A.; Dyndał, K.; Andrysiewicz, W.; Grochala, D.; Marszałek, K. GLAD Magnetron Sputtered Ultra-Thin Copper Oxide Films for Gas-Sensing Application. *Coatings* **2020**, *10*, 378. [[CrossRef](#)]
16. Rydosz, A. The Use of Copper Oxide Thin Films in Gas-Sensing Applications. *Coatings* **2018**, *8*, 425. [[CrossRef](#)]
17. Rydosz, A.; Szkudlarek, A. Gas-Sensing Performance of M-Doped CuO-Based Thin Films Working at Different Temperatures upon Exposure to Propane. *Sensors* **2015**, *15*, 20069–20085. [[CrossRef](#)]
18. Molavi, R.; Sheikhi, M.H. Materials Science in Semiconductor Processing Facile Wet Chemical Synthesis of Al Doped CuO Nanoleaves for Carbon Monoxide Gas Sensor Applications. *Mater. Sci. Semicond. Process.* **2020**, *106*, 104767. [[CrossRef](#)]
19. Choi, Y.; Kim, D.; Hong, S. Sensors and Actuators B: Chemical p-Type Aliovalent Li(I) or Fe(III)-Doped CuO Hollow Spheres Self-Organized by Cationic Complex Ink Printing: Structural and Gas Sensing Characteristics. *Sens. Actuators B Chem.* **2018**, *243*, 262–270. [[CrossRef](#)]
20. Wang, R.; Lin, S.; Liu, J. Li/Na-Doped CuO Nanowires and Nanobelts: Enhanced Electrical Properties and Gas Detection at Room Temperature. *J. Alloys Compd.* **2017**, *696*, 79–85. [[CrossRef](#)]
21. Alarrouqi, R.A.; Saleh, B.; Haik, Y.; Al-sulaiti, L.A. Selective Gas Sensors Using Graphene and CuO Nanorods. *Sens. Actuators A Phys.* **2018**, *283*, 107–112.
22. Hu, X.; Zhu, Z.; Chen, C.; Wen, T.; Zhao, X.; Xie, L. Highly Sensitive H<sub>2</sub>S Gas Sensors Based on Pd-Doped CuO Nanoflowers with Low Operating Temperature. *Sens. Actuators B Chem.* **2017**, *253*, 809–817. [[CrossRef](#)]
23. Lupan, O.; Postica, V.; Ababii, N.; Hoppe, M.; Cretu, V.; Tiginyanu, I.; Sontea, V.; Pauporté, T.; Viana, B.; Adelung, R. Influence of CuO Nanostructures Morphology on Hydrogen Gas Sensing Performances. *Microelectron. Eng.* **2016**, *164*, 63–70. [[CrossRef](#)]
24. Etape, E.P.; Ngolui, L.J.; Foba-tendo, J.; Yufanyi, D.M.; Namondo, B.V. Synthesis and Characterization of CuO, TiO<sub>2</sub>, and CuO-TiO<sub>2</sub> Mixed Oxide by a Modified Oxalate Route. *J. Appl. Chem.* **2017**, *2017*, 1–10. [[CrossRef](#)]
25. Ahamad, T.; Naushad, M.; Alshheri, S.M. Fabrication of Highly Porous N/S Doped Carbon Embedded with CuO/CuS Nanoparticles for NH<sub>3</sub> Gas Sensing. *Mater. Lett.* **2020**, *268*, 127515. [[CrossRef](#)]
26. Na, H.; Zhang, X.; Zhang, M.; Deng, Z.; Cheng, X.; Huo, L. Sensors and Actuators B: Chemical A Fast Response/ Recovery Ppb-Level H<sub>2</sub>S Gas Sensor Based on Porous CuO/ZnO Heterostructural Tubule via Con Fi Ned e Ff Ect of Absorbent Cotton. *Sens. Actuators B Chem.* **2019**, *297*, 126816. [[CrossRef](#)]
27. Wang, X.; Li, S.; Xie, L.; Li, X.; Lin, D.; Zhu, Z. Low-Temperature and Highly Sensitivity H<sub>2</sub>S Gas Sensor Based on ZnO/CuO Composite Derived from Bimetal Metal-Organic Frameworks. *Ceram. Int.* **2020**. [[CrossRef](#)]
28. Navale, Y.H.; Navale, S.T.; Stadler, F.J.; Ramgir, N.S.; Patil, V.B. Enhanced NO<sub>2</sub> Sensing Aptness of ZnO Nanowire/CuO Nanoparticle Heterostructure-Based Gas Sensors. *Ceram. Int.* **2018**, *45*, 1513–1522. [[CrossRef](#)]
29. Li, S.; Xie, L.; He, M.; Hu, X.; Luo, G.; Chen, C.; Zhu, Z. Metal-Organic Frameworks-Derived Bamboo-Like CuO/In<sub>2</sub>O<sub>3</sub> Heterostructure for High-Performance H<sub>2</sub>S Gas Sensor with Low Operating Temperature. *Sens. Actuators B Chem.* **2020**, *310*, 127828. [[CrossRef](#)]
30. Zhou, Y.; Wang, J.; Li, X. Flexible Room-Temperature Gas Sensor Based on Poly (Para-Phenylene Terephthalamide) Fibers Substrate Coupled with Composite NiO@CuO Sensing Materials for Ammonia Detection. *Ceram. Int.* **2020**, *46*, 13827–13834. [[CrossRef](#)]



31. Sui, L.; Yu, T.; Zhao, D.; Cheng, X.; Zhang, X.; Wang, P.; Xu, Y.; Gao, S.; Zhao, H.; Gao, Y.; et al. In Situ Deposited Hierarchical CuO/NiO Nanowall Arrays Film Sensor with Enhanced Gas Sensing Performance to H<sub>2</sub>S. *J. Hazard. Mater.* **2019**, *385*, 121570. [[CrossRef](#)] [[PubMed](#)]
32. He, M.; Xie, L.; Zhao, X.; Hu, X.; Li, S.; Zhu, Z. Highly Sensitive and Selective H<sub>2</sub>S Gas Sensors Based on Flower-like WO<sub>3</sub>/CuO Composites Operating at Low/Room Temperature. *J. Alloys Compd.* **2019**, *788*, 36–43. [[CrossRef](#)]
33. Sakthivel, B.; Nammalvar, G. Selective Ammonia Sensor Based on Copper Oxide/Reduced Graphene Oxide Nanocomposite. *J. Alloys Compd.* **2019**, *788*, 422–428. [[CrossRef](#)]
34. Li, Z.; Liu, Y.; Guo, D.; Guo, J.; Su, Y. Room-Temperature Synthesis of CuO/Reduced Graphene Oxide Nanohybrids for High-Performance NO<sub>2</sub> Gas Sensor. *Sens. Actuators B Chem.* **2018**, *271*, 306–310. [[CrossRef](#)]
35. Yang, B.; Liu, J.; Qin, H.; Liu, Q.; Jing, X.; Zhang, H.; Li, R. PtO<sub>2</sub> -Nanoparticles Functionalized CuO Polyhedrons for n-Butanol Gas Sensor Application. *Ceram. Int.* **2018**, *44*, 10426–10432. [[CrossRef](#)]
36. Park, S.; Cai, Z.; Lee, J.; Yoon, J., II; Chang, S. Fabrication of a Low-Concentration H<sub>2</sub>S Gas Sensor Using CuO Nanorods Decorated with Fe<sub>2</sub>O<sub>3</sub> Nanoparticles. *Mater. Lett.* **2016**, *181*, 231–235. [[CrossRef](#)]
37. Tan, W.; Yu, Q.; Ruan, X.; Huang, X. Design of SnO<sub>2</sub>-Based Highly Sensitive Ethanol Gas Sensor Based on Quasi Molecular-Cluster Imprinting Mechanism. *Sens. Actuators B Chem.* **2015**, *212*, 47–54. [[CrossRef](#)]
38. Ayesh, A.I.; Alyafei, A.A.; Anjum, R.S.; Mohamed, R.M.; Abuharb, M.B.; Salah, B.; El-muraikhi, M. Production of Sensitive Gas Sensors Using CuO/SnO<sub>2</sub> Nanoparticles. *Appl. Phys. A* **2019**, *125*, 550. [[CrossRef](#)]
39. Shang, Y.; Shi, W.; Zhao, R.; Ahmed, M.; Li, J.; Du, J. Simple Self-Assembly of 3D Laminated CuO/SnO<sub>2</sub> Hybrid for the Detection of Triethylamine. *Chin. Chem. Lett.* **2020**. [[CrossRef](#)]
40. Chen, T.; Chinnapaiyan, S.; Chen, S.; Ali, M.A.; Elshikh, M.S.; Mahmoud, A.H. Feasible Sonochemical Approach to Synthesize CuO@CeO<sub>2</sub> Nanomaterial and Their Enhanced Non-Enzymatic Sensor Performance towards Neurotransmitter. *Ultrason. Sonochem.* **2019**, *63*, 104903. [[CrossRef](#)]
41. Choi, S.; Park, J.Y.; Kim, S.S. Growth Behavior and Sensing Properties of Nanograins in CuO Nanofibers. *Chem. Eng. J.* **2011**, *172*, 550–556. [[CrossRef](#)]
42. Hou, L.; Zhang, C.; Li, L.; Du, C.; Li, X.; Kang, X.-F.; Chen, W. CO Gas Sensors Based on P-Type CuO Nanotubes and CuO Nanocubes: Morphology and Surface Structure Effects on the Sensing Performance. *Talanta* **2018**, *188*, 41–49. [[CrossRef](#)] [[PubMed](#)]
43. Shankar, P.; Bosco, J.; Rayappan, B. Gas Sensing Mechanism of Metal Oxides: The Role of Ambient Atmosphere, Type of Semiconductor and Gases-A Review. *Sci. Lett. J.* **2015**, *4*, 126.
44. Aslani, A.; Oroojpour, V. CO Gas Sensing of CuO Nanostructures, Synthesized by an Assisted Solvothermal Wet Chemical Route. *Phys. B Phys. Condens. Matter* **2011**, *406*, 144–149. [[CrossRef](#)]
45. Kim, J.; Katoch, A.; Choi, S.; Kim, S.S. Growth and Sensing Properties of Networked P-CuO Nanowires. *Sens. Actuators B Chem.* **2014**, *212*, 190–195. [[CrossRef](#)]
46. Nakate, U.T.; Hee, G.; Ahmad, R.; Patil, P.; Hahn, Y.; Yu, Y.T.; Suh, E. Nano-Bitter Gourd like Structured CuO for Enhanced Hydrogen Gas Sensor Application. *Int. J. Hydrogen Energy* **2018**, *43*, 22705–22714. [[CrossRef](#)]
47. Rodriguez, A.; Kim, J.Y.; Hanson, J.C.; Pe, M. Reduction of CuO in H<sub>2</sub>: In Situ Time-Resolved XRD Studies. *Catal. Lett.* **2003**, *85*, 247–254. [[CrossRef](#)]
48. Hermawan, A.; Asakura, Y.; Inada, M.; Yin, S. A Facile Method for Preparation of Uniformly Decorated-Spherical SnO<sub>2</sub> by CuO Nanoparticles for Highly Responsive Toluene Detection at High Temperature. *J. Mater. Sci. Technol.* **2020**, *51*, 119–129. [[CrossRef](#)]
49. Online, V.A.; Li, H.; Sun, Y.; Chang, F.; Deng, H.; Xie, L.; Li, H. High Sensitive Gas Sensor Based on CuO Nanoparticles Synthesized by Sol-Gel Method. *R. Soc. Chem.* **2016**, *6*, 79343–79349.
50. Varma, G.D. Enhanced Room Temperature Sensitivity of Ag-CuO Nanobrick/Reduced Graphene Oxide Composite for NO<sub>2</sub>. *J. Alloys Compd.* **2019**, *806*, 1469–1480.
51. Hozak, P.; Vorokhta, M.; Khalakhan, I.; Jarkovska, K.; Cibulkova, J.; Fitl, P.; Vlcek, J.; Fara, J.; Tomecek, D.; Vorokhta, M.; et al. New Insight into the Gas Sensing Properties of CuO<sub>x</sub> Nanowires by Near Ambient Pressure XPS New Insight into the Gas Sensing Properties of CuO<sub>x</sub> Nanowires by Near Ambient Pressure XPS. *J. Phys. Chem. C* **2019**, *123*, 29739–29749. [[CrossRef](#)]
52. Hu, J.; Zou, C.; Su, Y.; Li, M.; Han, Y.; Kong, E.S.W.; Yang, Z.; Zhang, Y. Ultrasensitive NO<sub>2</sub> Gas Sensor Based on Hierarchical Cu<sub>2</sub>O/CuO Mesocrystals Nanoflower. *J. Mater. Chem. A* **2018**, *6*, 17120–17131. [[CrossRef](#)]
53. Maximilian, F.; Meixner, H. Gallium Oxide Thin Films: A New Material for High-Temperature Oxygen Sensors. *Sens. Actuators B* **2000**, *4*, 437–441.

54. Roy, R.; Hill, V.G.; Osborn, E.F. Polymorphism of Ga<sub>2</sub>O<sub>3</sub> and the System Ga<sub>2</sub>O<sub>3</sub>-H<sub>2</sub>O. *J. Am. Chem. Soc.* **1952**, *74*, 719–722. [\[CrossRef\]](#)
55. Togashi, R.; Nomura, K.; Eguchi, C.; Fukizawa, T.; Goto, K.; Thieu, Q.T.; Murakami, H.; Kumagai, Y.; Kuramata, A.; Yamakoshi, S.; et al. Thermal Stability of β-Ga<sub>2</sub>O<sub>3</sub> in Mixed Flows of H<sub>2</sub> and N<sub>2</sub>. *Jpn. J. Appl. Phys.* **2015**, *54*, 041102. [\[CrossRef\]](#)
56. Mazeina, L.; Bermudez, V.M.; Perkins, F.K.; Arnold, S.P.; Prokes, S.M. Interaction of Functionalized Ga<sub>2</sub>O<sub>3</sub> NW-Based Room Temperature Gas Sensors with Different Hydrocarbons. *Sens. Actuators B Chem.* **2010**, *151*, 114–120. [\[CrossRef\]](#)
57. Chang, P.; Fan, Z.; Tseng, W.; Rajagopal, A.; Lu, J.G.; Chang, P.; Fan, Z.; Tseng, W.; Rajagopal, A.; Lu, J.G. β-Ga<sub>2</sub>O<sub>3</sub> Nanowires: Synthesis, Characterization, and p-Channel Field-Effect Transistor. *Appl. Phys. Lett.* **2009**, *222102*, 88–91. [\[CrossRef\]](#)
58. Zheng, S.U.N.; Linhong, Y.; Xuechu, S.; Zhanghai, C. Anisotropic Raman Spectroscopy of a Single Ga<sub>2</sub>O<sub>3</sub> Nanobelt. *Chin. Sci. Bull.* **2012**, *57*, 565–568.
59. Zhang, Z.; Wang, X. Phase Transition of Two-Dimensional β-Ga<sub>2</sub>O<sub>3</sub> Nanosheets from Ultrathin γ-Ga<sub>2</sub>O<sub>3</sub> Nanosheets and Their Photocatalytic Hydrogen Evolution Activities. *ACS Omega* **2018**, *3*, 14469–14476. [\[CrossRef\]](#)
60. Guo, D.; Guo, Q.; Chen, Z.; Wu, Z.; Li, P.; Tang, W. Review of Ga<sub>2</sub>O<sub>3</sub>-Based Optoelectronic Devices. *Mater. Today Phys.* **2019**, *11*, 100157. [\[CrossRef\]](#)
61. Nakagomi, S.; Sai, T.; Kokubun, Y. Hydrogen Gas Sensor with Self Temperature Compensation Based on β-Ga<sub>2</sub>O<sub>3</sub> Thin Film. *Sens. Actuators B Chem.* **2013**, *187*, 413–419. [\[CrossRef\]](#)
62. Orita, M.; Hiramatsu, H.; Ohta, H.; Hirano, M.; Hosono, H. Preparation of Highly Conductive, Deep Ultraviolet Transparent Ga<sub>2</sub>O<sub>3</sub> Thin Film at Low Deposition Temperatures. *Thin Solid Films* **2002**, *411*, 134–139. [\[CrossRef\]](#)
63. Cuong, N.D.; Park, Y.W.; Yoon, S.G. Microstructural and Electrical Properties of Ga<sub>2</sub>O<sub>3</sub> Nanowires Grown at Various Temperatures by Vapor-Liquid-Solid Technique. *Sens. Actuators B Chem.* **2009**, *140*, 240–244. [\[CrossRef\]](#)
64. Frank, J.; Fleischer, M.; Meixner, H. Gas-Sensitive Electrical Properties of Pure and Doped Semiconducting Ga<sub>2</sub>O<sub>3</sub> Thick Films. *Sens. Actuators B Chem.* **1998**, *48*, 318–321. [\[CrossRef\]](#)
65. Shan, F.K.; Liu, G.X.; Lee, W.J.; Lee, G.H.; Kim, I.S.; Shan, F.K.; Liu, G.X.; Lee, W.J.; Lee, G.H.; Kim, I.S.; et al. Structural, Electrical, and Optical Properties of Transparent Gallium Oxide Thin Films Grown by Plasma-Enhanced Atomic Layer Deposition. *J. Appl. Phys.* **2005**, *98*, 023504. [\[CrossRef\]](#)
66. Shi, Q.; Wang, Q.; Zhang, D.; Wang, Q.; Li, S.; Wang, W.; Fan, Q.; Zhang, J. Structural, Optical and Photoluminescence Properties of Ga<sub>2</sub>O<sub>3</sub> Thin Films Deposited by Vacuum Thermal Evaporation. *J. Lumin.* **2019**, *206*, 53–58. [\[CrossRef\]](#)
67. Hoefer, U.; Frank, J.; Fleischer, M. High Temperature Ga<sub>2</sub>O<sub>3</sub>-Gas Sensors and SnO<sub>2</sub>-Gas Sensors: A Comparison. *Sens. Actuators B Chem.* **2001**, *78*, 6–11. [\[CrossRef\]](#)
68. Wang, J.; Ye, L.; Wang, X.; Zhang, H.; Li, L.; Kong, C.; Li, W. High Transmittance β-Ga<sub>2</sub>O<sub>3</sub> Thin Films Deposited by Magnetron Sputtering and Post-Annealing for Solar-Blind Ultraviolet Photodetector. *J. Alloys Compd.* **2019**, *803*, 9–15. [\[CrossRef\]](#)
69. Yusa, S.; Oka, D.; Fukumura, T. High κ dielectric ε-Ga<sub>2</sub>O<sub>3</sub> Stabilized in a Transparent Heteroepitaxial Structure Grown by Mist CVD at Atmospheric Pressure. *CrystEngComm* **2019**, *22*, 381–385. [\[CrossRef\]](#)
70. Higashiwaki, M.; Sasaki, K.; Kuramata, A.; Masui, T.; Yamakoshi, S. Development of Gallium Oxide Power Devices. *Phys. Status Solidi Appl. Mater. Sci.* **2014**, *211*, 21–26. [\[CrossRef\]](#)
71. Frank, J.; Fleischer, M.; Meixner, H.; Feltz, A. Enhancement of Sensitivity and Conductivity of Semiconducting Ga<sub>2</sub>O<sub>3</sub> Gas Sensors by Doping with SnO<sub>2</sub>. *Sens. Actuators B Chem.* **1998**, *49*, 110–114. [\[CrossRef\]](#)
72. Li, Y.; Trinchi, A.; Wlodarski, W.; Galatsis, K.; Kalantar-Zadeh, K. Investigation of the Oxygen Gas Sensing Performance of Ga<sub>2</sub>O<sub>3</sub> Thin Films with Different Dopants. *Sens. Actuators B Chem.* **2003**, *93*, 431–434. [\[CrossRef\]](#)
73. Afzal, A. β-Ga<sub>2</sub>O<sub>3</sub> Nanowires and Thin Films for Metal Oxide Semiconductor Gas Sensors: Sensing Mechanisms and Performance Enhancement Strategies. *J. Mater.* **2019**, *5*, 542–557. [\[CrossRef\]](#)
74. Nagarajan, V.; Chandiramouli, R. Methane Adsorption Characteristics on β-Ga<sub>2</sub>O<sub>3</sub> Nanostructures: DFT Investigation. *Appl. Surf. Sci.* **2015**, *344*, 65–78. [\[CrossRef\]](#)

75. Wu, N.; Chen, Z.; Xu, J.; Chyu, M.; Mao, S.X. Impedance-Metric Pt/YSZ/Au-Ga<sub>2</sub>O<sub>3</sub> Sensor for CO Detection at High Temperature. *Sens. Actuators B Chem.* **2005**, *110*, 49–53. [[CrossRef](#)]
76. Mohammadi, M.R.; Fray, D.J. Semiconductor TiO<sub>2</sub>-Ga<sub>2</sub>O<sub>3</sub> Thin Film Gas Sensors Derived from Particulate Sol-Gel Route. *Acta Mater.* **2007**, *55*, 4455–4466. [[CrossRef](#)]
77. Weh, T.; Frank, J.; Fleischer, M.; Meixner, H. On the Mechanism of Hydrogen Sensing with SiO<sub>2</sub> Modified High Temperature Ga<sub>2</sub>O<sub>3</sub> Sensors. *Sens. Actuators B Chem.* **2001**, *78*, 202–207. [[CrossRef](#)]
78. Jang, Y.G.; Kim, W.S.; Kim, D.H.; Hong, S.H. Fabrication of Ga<sub>2</sub>O<sub>3</sub>/SnO<sub>2</sub> Core-Shell Nanowires and Their Ethanol Gas Sensing Properties. *J. Mater. Res.* **2011**, *26*, 2322–2327. [[CrossRef](#)]
79. Park, S.; Kim, S.; Sun, G.; Lee, C. Synthesis, Structure and Ethanol Sensing Properties of Ga<sub>2</sub>O<sub>3</sub>-Core/WO<sub>3</sub>-Shell Nanostructures. *Thin Solid Films* **2015**, *591*, 341–345. [[CrossRef](#)]
80. Janowitz, C.; Scherer, V.; Mohamed, M.; Krapf, A.; Dwelk, H.; Manzke, R.; Galazka, Z.; Uecker, R.; Irmscher, K.; Fornari, R. Experimental electronic structure of In<sub>2</sub>O<sub>3</sub> and Ga<sub>2</sub>O<sub>3</sub>. *New J. Phys.* **2011**, *13*, 085014. [[CrossRef](#)]
81. Jin, C.; Park, S.; Kim, H.; Lee, C. Ultrasensitive Multiple Networked Ga<sub>2</sub>O<sub>3</sub>-Core/ZnO-Shell Nanorod Gas Sensors. *Sens. Actuators B Chem.* **2012**, *161*, 223–228. [[CrossRef](#)]
82. Frank, J.; Fleischer, M.; Meixner, H. Electrical Doping of Gassensitive, Semiconducting Ga<sub>2</sub>O<sub>3</sub> Thin Films. *Sens. Actuators B Chem.* **1996**, *34*, 373–377. [[CrossRef](#)]
83. Pohle, R.; Fleischer, M.; Meixner, H. In Situ Infrared Emission Spectroscopic Study of the Adsorption of H<sub>2</sub>O and Hydrogen-Containing Gases on Ga<sub>2</sub>O<sub>3</sub> Gas Sensors. *Sens. Actuators B Chem.* **2000**, *68*, 151–156. [[CrossRef](#)]
84. Manandhar, S.; Battu, A.K.; Devaraj, A.; Shutthanandan, V.; Thevuthasan, S.; Ramana, C.V. Rapid Response High Temperature Oxygen Sensor Based on Titanium Doped Gallium Oxide. *Sci. Rep.* **2020**, *10*, 1–9. [[CrossRef](#)]
85. Schwebel, T.; Fleischer, M.; Meixner, H.; Kohl, C.D. CO-Sensor for Domestic Use Based on High Temperature Stable Ga<sub>2</sub>O<sub>3</sub> Thin Films. *Sens. Actuators B Chem.* **1998**, *49*, 46–51. [[CrossRef](#)]
86. Pilliadugula, R.; Krishnan, N.G. Effect of PH Dependent Morphology on Room Temperature NH<sub>3</sub> Sensing Performances of β-Ga<sub>2</sub>O<sub>3</sub>. *Mater. Sci. Semicond. Process.* **2020**, *112*, 105007. [[CrossRef](#)]
87. Pandeewari, R.; Jeyaprakash, B.G. High Sensing Response of β-Ga<sub>2</sub>O<sub>3</sub> Thin Film towards Ammonia Vapours: Influencing Factors at Room Temperature. *Sens. Actuators B Chem.* **2014**, *195*, 206–214. [[CrossRef](#)]
88. Li, Z.; Jiao, T.; Hu, D.; Lv, Y.; Li, W.; Dong, X.; Zhang, Y.; Feng, Z.; Zhang, B. Study on β-Ga<sub>2</sub>O<sub>3</sub> Films Grown with Various VI/III Ratios by MOCVD. *Coatings* **2019**, *9*, 281. [[CrossRef](#)]
89. Winkler, S.N.; Dimopoulos, T. Nanocrystalline Ga<sub>2</sub>O<sub>3</sub> Films Deposited by Spray Pyrolysis from Water-Based Solutions on Glass and TCO Substrates. *J. Mater. Chem. C* **2019**, *7*, 69–77. [[CrossRef](#)]
90. Arias, A.; Nedev, N.; Ghose, S.; Rojas-ramirez, J.S.; Mateos, D.; Alvarez, M.C.; Oscar, P.; Su, M.; Valdez-salas, B.; Droopad, R. Structural, Optical, and Electrical Characterization of β-Ga<sub>2</sub>O<sub>3</sub> Thin Films Grown by Plasma-Assisted Molecular Beam Epitaxy Suitable for UV Sensing. *Adv. Mater. Sci. Eng.* **2018**, *2018*, 1–6. [[CrossRef](#)]
91. Yang, C.; Xu, J.; Yan, L.; Cai, C.; Liu, W. Effects of Depositing Temperature on Structural, Optical and Laser-Induced Damage Properties of Ga<sub>2</sub>O<sub>3</sub> Films Deposited by Electronic Beam Evaporation. *Opt. Laser Technol.* **2019**, *113*, 192–197. [[CrossRef](#)]
92. Berencén, Y.; Xie, Y.; Wang, M.; Prucnal, S.; Rebohle, L.; Zhou, S. Structural and Optical Properties of Pulsed-Laser Deposited Crystalline β-Ga<sub>2</sub>O<sub>3</sub> Thin Films on Silicon. *Semicond. Sci. Technol.* **2019**, *34*, 035001. [[CrossRef](#)]
93. Cheah, L.B.; Aina, R.; Osman, M.; Poopalan, P. Ga<sub>2</sub>O<sub>3</sub> Thin Films by Sol-Gel Method Its Optical Properties. In Proceedings of the 2nd International Conference on Applied Photonics and Electronics 2019 (InCAPE 2019), Putrajaya, Malaysia, 22 August 2019; Volume 2203, pp. 020028-1–020028-6.
94. Wei, Z.; Akbari, M.K.; Hai, Z.; Ramachandran, R.K.; Detavernier, C.; Verpoort, F.; Kats, E.; Xu, H.; Hu, J.; Zhuiykov, S. Ultra-Thin Sub-10 Nm Ga<sub>2</sub>O<sub>3</sub>-WO<sub>3</sub> Heterostructures Developed by Atomic Layer Deposition for Sensitive and Selective C<sub>2</sub>H<sub>5</sub>OH Detection on Ppm Level. *Sens. Actuators B Chem.* **2019**, *287*, 147–156. [[CrossRef](#)]
95. Rafea, M.A.; Roushdy, N. Determination of the Optical Band Gap for Amorphous and Nanocrystalline Copper Oxide Thin Films Prepared by SILAR Technique. *J. Phys. D Appl. Phys.* **2009**, *42*, 015413. [[CrossRef](#)]
96. Dahrul, M.; Alatas, H. Preparation and Optical Properties Study of CuO Thin Film as Applied Solar Cell on LAPAN-IPB Satellite. *Procedia Environ. Sci.* **2016**, *33*, 661–667. [[CrossRef](#)]

97. Flingelli, G.K.; Fleischer, M.M.; Meixner, H. Selective Detection of Methane in Domestic Environments Using a Catalyst Sensor System Based on Ga<sub>2</sub>O<sub>3</sub>. *Sensors Actuators, B Chem.* **1998**, *48*, 258–262. [[CrossRef](#)]
98. Wang, J.; Jiang, S.; Liu, H.; Wang, S.; Pan, Q.; Yin, Y.; Zhang, G. P-Type Gas-Sensing Behavior of Ga<sub>2</sub>O<sub>3</sub>/Al<sub>2</sub>O<sub>3</sub> Nanocomposite with High Sensitivity to NO<sub>x</sub> at Room Temperature. *J. Alloys Compd.* **2020**, *814*, 152284. [[CrossRef](#)]
99. Liu, Z.; Yamazaki, T.; Shen, Y.; Kikuta, T.; Nakatani, N.; Li, Y. O<sub>2</sub> and CO Sensing of Ga<sub>2</sub>O<sub>3</sub> Multiple Nanowire Gas Sensors. *Sens. Actuators B Chem.* **2008**, *129*, 666–670. [[CrossRef](#)]
100. Rydosz, A. Amorphous and Nanocrystalline Magnetron Sputtered CuO Thin Films Deposited on Low Temperature Cofired Ceramics Substrates for Gas Sensor Applications. *IEEE Sens. J.* **2014**, *14*, 1600–1607. [[CrossRef](#)]
101. Krzeminski, W.A.J.; Marszalek, K.S.K.; Rydosz, M.S.A. Flexible Gas Sensor Printed on a Polymer Substrate for Sub-Ppm Acetone Detection. *Electron. Mater. Lett.* **2020**, *16*, 146–155.
102. Krupinski, M.; Perzanowski, M.; Polit, A.; Zabala, Y.; Zarzycki, A.; Dobrowolska, A.; Marszalek, M. X-Ray Absorption Fine Structure and x-Ray Diffraction Studies of Crystallographic Grains in Nanocrystalline FePd:Cu Thin Films. *J. Appl. Phys.* **2011**, *109*, 064306. [[CrossRef](#)]
103. Perzanowski, M.; Krupinski, M.; Zarzycki, A.; Zabala, Y.; Marszalek, M. Determination of Grain Shape of Laser-Irradiated FePdCu Thin Alloy Films. *Appl. Surf. Sci.* **2014**, *302*, 129–133. [[CrossRef](#)]
104. Rodríguez-Carvajal, J. Recent Developments of the Program Full prof. *Comm. Powder Diffr. (IUCr)* **2001**, *26*, 12–19.



© 2020 by the authors. Licensee MDPI, Basel, Switzerland. This article is an open access article distributed under the terms and conditions of the Creative Commons Attribution (CC BY) license (<http://creativecommons.org/licenses/by/4.0/>).